Journal of Solid State Chemistry 184 (2011) 2799–2805

Contents lists available at SciVerse ScienceDirect

Journal of Solid State Chemistry

journal homepage: www.elsevier.com/locate/jssc

Nanocrystalline ferrites $Ni_xZn_{1-x}Fe_2O_4$: Influence of cation distribution on acidic and gas sensing properties

A.P. Kazin [a], M.N. Rumyantseva [a,*], V.E. Prusakov [b], I.P. Suzdalev [b], A.M. Gaskov [a]

[a] Chemistry Department, Moscow State University, Leninskie Gory 1-3, 119991 Moscow, Russia
[b] Institute of Chemical Physics, 119991 Moscow, Russia

ARTICLE INFO

Article history:
Received 26 May 2011
Received in revised form
15 August 2011
Accepted 22 August 2011
Available online 26 August 2011

Keywords:
Aerosol pyrolysis
Zinc nickel ferrite
Mössbauer spectroscopy
Surface acidic properties
Gas sensor properties

ABSTRACT

This work is devoted to a detailed analysis of the interconnection between composition, cation distribution and acidic properties of the surface of nanocrystalline ferrites $Ni_xZn_{1-x}Fe_2O_4$ obtained by aerosol pyrolysis. The detailed analysis of the Mössbauer spectra allows us to determine the distribution of cations between tetrahedral and octahedral positions in spinel structure. Depending on samples composition, the tetrahedral positions can be occupied by only Fe^{3+} cations (inverse spinel, $x \geq 0.4$) or by Fe^{3+} and Zn^{2+} cations (mixed spinel, $x=0$, 0.2). Increasing the nickel concentration in the ferrite leads to decrease in the number of strong acid centers on the surface. It was found that the decrease in the contribution of strong surface acid sites leads to an increase in sensory sensitivity of the ferrite towards ammonia. For ethanol detection an inverse relationship between sensor signal and surface acidity was observed.

© 2011 Elsevier Inc. All rights reserved.

1. Introduction

Despite the fact that ferrites of the metals are one of the most studied groups of materials and produce a wide industry for electromagnetic devices, an exceptional interest in investigation of these materials in a nanocrystalline state with high surface area for chemical sensors is observed [1]. The main advantage of complex ferrites compared to traditional sensor materials based on semiconductor metal oxides is the ability to regulate the nature of active sites on their surface by changing the cation composition. The main conclusion of the published work to date is the discovery of the high sensitivity of the functional properties of the ferrites to the cation composition and microstructure: grain size and pores, the specific surface of materials. All these parameters are determined by the synthesis conditions. Methods of preparation of nanocrystalline ferrites are currently under intensive development based on various technologies of "soft chemistry". Of greatest interest are methods of hydrothermal synthesis [2], co-deposition from solution [3], thermal decomposition of oxoacetates [4], as well as aerosol pyrolysis [5]. The main advantages of the later synthesis method are the wide spectrum of suitable precursors, possibility to make a synthesis in an aqueous or organic media, effective control of composition during the synthesis of complex multicomponent powders or films.

This work is devoted to a detailed analysis of the interconnection between composition, cation distribution and acidic properties of the surface of nanocrystalline ferrites $Ni_xZn_{1-x}Fe_2O_4$ ($x=0$, 0.2, 0.4, 0.6, 0.8, 1), obtained by pyrolysis of aerosols, in relation to gas sensor properties of these materials towards NH_3 and ethanol vapor.

2. Experimental

Complex nanocrystalline ferrites $Ni_xZn_{1-x}Fe_2O_4$ ($x=0$, 0.2, 0.4, 0.6, 0.8, 1) were synthesized using spray pyrolysis. The spray pyrolysis reactor included a temperature-programmed (up to 800 °C) tube furnace, an Al'bedo IN-72 ultrasonic generator, a carrier-gas flow control system, and an electrostatic filter.

The starting chemicals used were $Fe(NO_3)_3 \cdot 9H_2O$, $Ni(NO_3)_2 \cdot 6H_2O$, and $Zn(NO_3)_2 \cdot 6H_2O$ (Fluka). Aqueous nitrate solutions were mixed to give a [Ni]:[Fe]:[Zn] appropriate molar ratio and were then diluted to a ([Ni]+[Fe]+[Zn])=0.2 M concentration. This aqueous solution was atomized by sonication, and the aerosol was delivered by a carrier gas (atmospheric air) to a tubular quartz reactor, where the nitrates decomposed at 800 °C to form ferrite. The ferrite's particles were collected on the plates of the electrostatic filter in the form of fine powder. The powders were annealed in air for 24 h at 500 °C to obtain materials, which are similar in particle size.

The elemental composition of the powders was determined by laser mass spectrometry (LMS) with an EMAL-2 instrument. X-ray

* Corresponding author. Fax: +7 495 939 09 98.
E-mail address: roum@inorg.chem.msu.ru (M.N. Rumyantseva).

0022-4596/$ - see front matter © 2011 Elsevier Inc. All rights reserved.
doi:10.1016/j.jssc.2011.08.029

diffraction (XRD) patterns were collected on a Rigaku diffractometer (monochromatized Cu$K\alpha$ radiation, $\lambda=1.5406$ Å). The morphology and particle size of the powders were determined on a LEO SUPRA 50VP field emission scanning electron microscope (SEM) (Carl Zeiss, Germany). The specific surface area (S_{BET}) of the powders was determined by low temperature nitrogen adsorption (BET analysis, Micromeritics Chemisorb 2750). The parameters of synthesized ferrites are given in Table 1.

The Mössbauer spectra were collected at temperatures from 16 to 300 K on an electrodynamic spectrometer (Wissel, Germany) using a Janis CCS-850 He cryostat with a Lake Shore Cryogenics Model 332 temperature controller. The temperature was maintained with a stability of 0.1 K. The gamma source used was ^{57}Co(Rh) with an activity of 1.1 GBq. The isomer shift was determined relative to the center of the magnetic hyperfine structure of α-Fe at 300 K. The spectra were analyzed by a least squares fitting assuming the Lorentzian lineshapes.

The acidic properties of the surface of synthesized ferrites were characterized by NH_3 temperature-programmed desorption (NH_3-TPD, Micromeritics Chemisorb 2750). Before the experiments, the samples were pretreated for 2 h at 400 °C in a flow of helium. Adsorption of NH_3 was performed at room temperature using NH_3:N_2=1:1 gas mixture. NH_3–TPD was carried out in helium flow after purging the sample at 50 °C for 60 min to decrease the amount of physisorbed ammonia. The temperature was increased with a rate of 8 °C/min up to 800 °C. Total amount of acid sites (***A***) was determined from the NH_3–TPD curves, supposing that one NH_3 molecule desorbes from each site.

For the gas sensing experiments, the materials were deposited in form of thick films over functional substrates, provided with Pt contacts on the front side and a Pt-meander that acts both as heating element and temperature probe, on the back-side. During the measurements the substrate temperature was maintained constant at 350 °C. All measurements have been carried out by flow through technique under controlled constant flux of 100 ml/min. The atmosphere composition was preassigned by means of electronic mass-flow controllers (Bronkhorst), mixing flows coming from certified bottles containing a given amount of the target gas diluted in synthetic air with the background flow. The background atmosphere was generated from a dry air certified bottle. The sensors were exposed to a constant concentration of target gas for 30 min and then to the background atmosphere for 90 min.

DC volt–amperometric measurements ($U=3$ V) have been carried out to monitor samples' electrical conductance during exposure to NH_3 (12.5 ppm in dry air) and ethanol vapor (29 ppm in dry air). The response S of the sensor was calculated as

$$S=\frac{G_{gas}}{G_0} \text{ for } n\text{-type samples and } S=\frac{G_0}{G_{gas}} \text{ for } p\text{-type samples,} \quad (1)$$

where G_{gas} is conductance in the presence of target gas and G_0 is conductance in the background air.

Table 1
Microstructure parameters and acidic properties of $Ni_xZn_{1-x}Fe_2O_4$ samples.

x in $Ni_xZn_{1-x}Fe_2O_4$	Crystallite size d_{XRD} (nm)	Specific surface area S_{BET} (m^2/g)	Agglomerate size d_{BET} (nm)	Density of acid centers A/S_{BET} (10^{-6} mole/m^2)	ΣICP
0	9 ± 1	6 ± 2	194	24 ± 5	1.887
0.2	10 ± 1	11 ± 2	101	15 ± 3	1.876
0.4	11 ± 1	13 ± 2	84	6 ± 1	1.866
0.6	12 ± 1	28 ± 1	40	4.0 ± 0.5	1.851
0.8	17 ± 2	25 ± 2	45	3.5 ± 0.5	1.837
1.0	17 ± 2	28 ± 1	40	5.0 ± 0.5	1.823

3. Results and discussion

According to scanning electron microscopy the powders synthesized by spray pyrolysis are characterized by hierarchical structure (Fig. 1): nanocrystals agglomerate into large porous particles of 0.1–2 μm in diameter with almost perfectly spherical shape. Particles with an average diameter of 250–600 nm are dominating. From the micrographs one can conclude that zinc ferrite particles (Fig. 1a) have a smoother surface than the particles of nickel ferrite (Fig. 1b). The average size of spherical particles and their size distribution does not depend on the composition of the ferrites, plausible these parameters are determined by size of aerosol droplets formed during the synthesis. There is an evidence [6], that the droplet size depends on viscosity, surface tension, and density of the solution, as well as the frequency of ultrasonic generator. Since the nature of solvent (water), total salts concentration in solutions, and parameters of ultrasonic generator were the same in all experiments, there is no reason to expect any difference in the size of aerosol droplets.

According to LMS data the chemical composition of ferrites $Ni_xZn_{1-x}Fe_2O_4$ is close to the targeted one for most part of samples with the exception for $x=0$ and $x=0.6$ (Fig. 2). In these cases the increased [Zn]/[Fe] ratio is observed, which can result in ZnO phase formation. However XRD spectra demonstrate that all the samples are single phase and consist of ferrites $Ni_xZn_{1-x}Fe_2O_4$ with the spinel structure (Fig. 3). This may be due to low content or poor crystallinity of ZnO phase. With the increase of nickel concentration in $Ni_xZn_{1-x}Fe_2O_4$ the average crystallite size (d_{XRD})

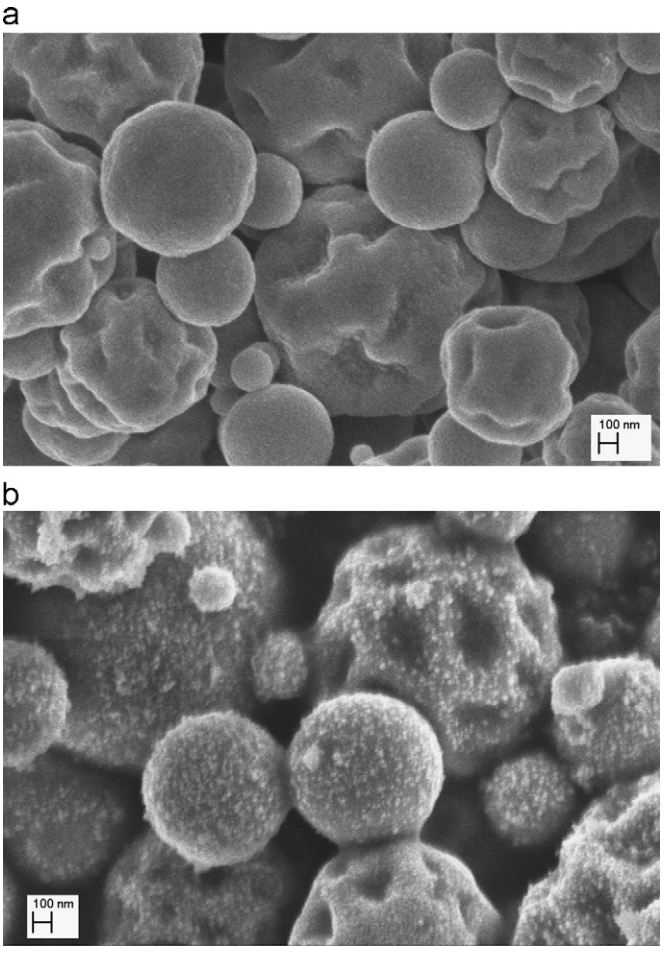

Fig. 1. SEM micrographs of synthesized samples: (a) $ZnFe_2O_4$ and (b) $NiFe_2O_4$. Magnification 50000 × .

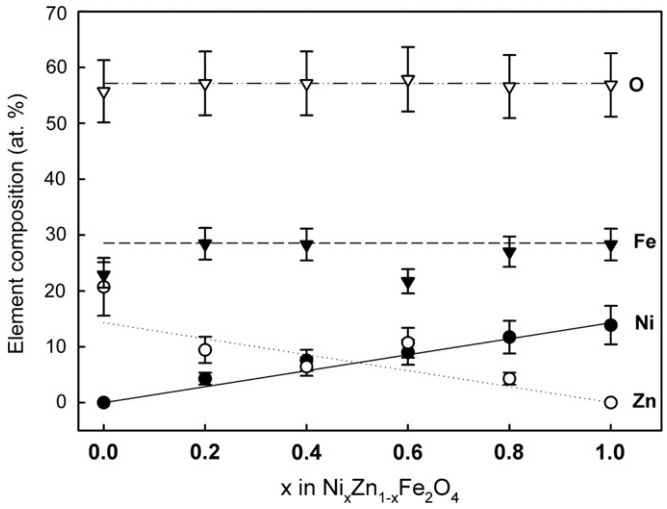

Fig. 2. Atomic part of elements in $Ni_xZn_{1-x}Fe_2O_4$ (LMS). Lines depict the values corresponding to targeted composition.

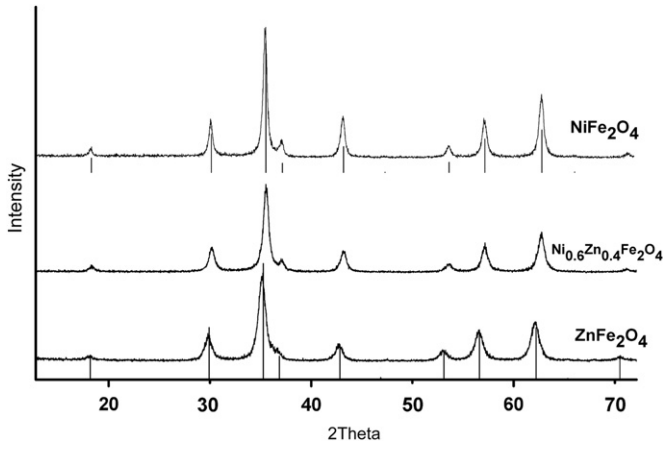

Fig. 3. X-ray diffraction patterns of synthesized $Ni_xZn_{1-x}Fe_2O_4$ samples. Vertical lines correspond to $NiFe_2O_4$ (ICDD 74-2084) and $ZnFe_2O_4$ (ICDD 77-11) phases.

of spinel phase estimated by the Scherrer formula, increases from 9 to 17 nm and the lattice parameter a decreases monotonically from the value characteristic for $ZnFe_2O_4$ (8.416 Å, ICDD 77-11) to the one characteristic for $NiFe_2O_4$ (8.338 Å, ICDD 74-2081) (Table 1). This change in lattice parameter correlates with the ionic radii of cations occupying the tetrahedral sites A in spinel structure for $Zn_A[FeFe]_BO_4$ and $Fe_A[NiFe]_BO_4$: $r(Zn^{2+})=0.60$ Å, $r(Fe^{3+})=0.49$ Å [7]. It is necessary to note that for intermediate compositions there is a deviation from Vegard's law (Fig. 4).

It was demonstrated in our previous work [8] that due to the synthesis method the obtained $NiFe_2O_4$ with hierarchical porous structure is characterized by a considerable specific surface area. For the series of ferrites $Ni_xZn_{1-x}Fe_2O_4$ the specific surface area determined from low temperature nitrogen adsorption (S_{BET}) decreases with the decrease of Ni concentration (Table 1). Surprisingly, this decrease of S_{BET} corresponds to the decrease of crystallite size d_{XRD}. The obtained values of S_{BET} allow estimating the effective size of agglomerates, whose surface is really open for gas adsorption using a simple geometrical approach of spherical particle shape[1]:

$$d_{BET} = \frac{6 \times 1000}{\rho S_{BET}}, \quad (2)$$

[1] Specific surface area of a spherical particle of diameter d is $S_{BET} = (S/m) = (S/\rho V) = (\pi d^2/\rho(\pi d^3/6)) = (6/\rho d)$, where S is the surface area of a sphere, V is volume of a sphere, m is mass, and ρ is density. Taking into consideration the dimensions of S_{BET} (m^2/g), ρ (g/cm^3) and d (nm), one can obtain the ratio (2).

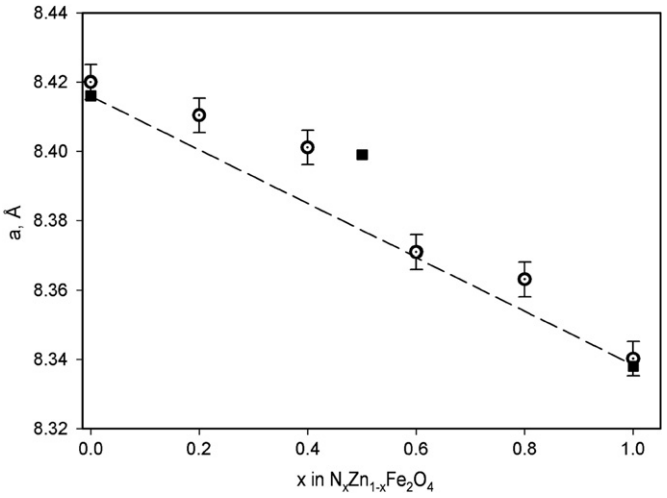

Fig. 4. Lattice parameter a of the phase with spinel structure depending on the composition of ferrite $Ni_xZn_{1-x}Fe_2O_4$. Symbols ■ mark the literature data (ICDD) for the corresponding ferrite composition.

where d_{BET} (nm) is this equivalent size or BET size, ρ (g/cm^3) = ($MZ/VN_A \times 10^{-24}$) is the theoretical density of the crystalline ferrite $Ni_xZn_{1-x}Fe_2O_4$, M (amu) is molecular mass, Z is number of formula units, V (Å^3) is volume of elementary cell, and N_A is Avogadro's number.

It should be noted that the size of the agglomerates d_{BET} determined for $ZnFe_2O_4$ (about 200 nm) is comparable with the size of spherical particles identified by SEM (250–650 nm). This indicates that the powder of zinc ferrite consists of the dense particles, the inner surface of which is not accessible for gas molecules. Increase in nickel content leads to decrease of d_{BET} (Table 1) indicating the partial gas permeability of spherical particles. So we have to note that smaller crystallites of $Ni_xZn_{1-x}Fe_2O_4$ form denser aggregates. Such tendency in sintering of nickel zinc ferrites can be due to differences in thermal decomposition of $Ni(NO_3)_2$ and $Zn(NO_3)_2$ [9,10].

The Mössbauer spectra of all nanocrystalline samples $Ni_xZn_{1-x}Fe_2O_4$ demonstrate progressive transition from electric-quadrupole to magnetic hyperfine (HF) interaction with decrease of temperature and increase of nickel portion. The Mössbauer spectrum (MS) of nano-sized $ZnFe_2O_4$ at $T=300$ K (Fig. 5) is a paramagnetic quadrupole doublet with the parameters: isomer shift, $\delta=0.36$ mm/s, quadrupole splitting, $\Delta E_Q=0.50$ mm/s, linewidth, $\Gamma_{1/2}=0.51$ mm/s. Such doublet spectrum at 300 K is also characteristic of bulk $ZnFe_2O_4$ samples [11,12]. Bulk zinc ferrite $ZnFe_2O_4$ has the structure of normal spinel, where tetrahedral (A) positions are fully occupied by diamagnetic ions Zn^{2+}, and octahedral (B) –by Fe^{3+} ions, and is an antiferromagnet with a Néel temperature of 10 K. Above this temperature, $ZnFe_2O_4$ demonstrates an abrupt transition into the paramagnetic state [12]. In addition, the doublet spectrum of $ZnFe_2O_4$ with crystallite size of 9 nm can be attributed to size effects [8,13–15]. At 80 K the main components of MS of nanosized $ZnFe_2O_4$ is also a doublet (relative weight $G \approx 70\%$) with broadened components ($\Gamma_{1/2} \approx 0.81$ mm/s). Along with the doublet in the spectrum there is an unresolved magnetic component, which may be a consequence of partly inverted population of the lattice by Fe^{3+}. Similar doublet spectra at 300 and 80 K were observed in [16] for nano-sized $ZnFe_2O_4$ with an average particle size of 9 nm. At 16 K in the MS one can distinguish two magnetic hyperfine

structures (sextets with content of 30% and 70% in area), which can be attributed to the formation of mixed spinel $(Zn_{0.4}Fe_{0.6})_A[Zn_{0.6}Fe_{1.4}]_BO_4$. The values of magnetic hyperfine field, B_{in}, for *A* and *B* positions are, respectively, 41.5 and 47.8 T, which is much smaller than the corresponding values for $NiFe_2O_4$ with similar crystallite size – 47.7 and 51.8 T, respectively [8].

In MS of nanosized $Ni_{0.2}Zn_{0.8}Fe_2O_4$ at 300 K we also observed a paramagnetic doublet, but with a slightly larger linewidth $\Gamma_{1/2} \approx 0.56$ mm/s. This can be explained as by the important contribution of normal spinel structure with a high content of non-magnetic Zn^{2+} in the *B* position and by size effects ($d_{XRD}=10$ nm). At 80 K MS demonstrates the magnetic HFS with broad lines, indicating a partially inverted nature of the spinel structure. At 16 K in MS one can distinguish two magnetic HFS (with relative weight *G* about 40% and 60%), corresponding to Fe^{3+}, respectively, in *A* and *B* positions of the mixed spinel. The Mössbauer parameters at $T=16$ K for all samples $Ni_xZn_{1-x}Fe_2O_4$ are presented in Table 2.

MS of $Ni_{0.4}Zn_{0.6}Fe_2O_4$ at 300 K is a superposition of a doublet ($G \approx 15\%$) and a nonresolved magnetic HFS. The doublet components are essentially broadened relative to corresponding doublets for $ZnFe_2O_4$ and $Ni_{0.2}Zn_{0.8}Fe_2O_4$. The presence of the magnetic HFS at 300 K can be indicative of a larger average size (11 nm) of crystallites in the sample comparing with studied earlier [8] $NiFe_2O_4$ with crystallite size of 9 nm. The spectra registered at 78 and 16 K are well fitted with two sextets with broadened components with about equal content that can be explained with formation of the fully inverted spinel structure.

The further increase of Ni portion in $Ni_xZn_{1-x}Fe_2O_4$ ferrites leads to a disappearance of paramagnetic doublets in the Mössbauer spectra. MS of $Ni_{0.6}Zn_{0.4}Fe_2O_4$ at 300 K is a superposition of two poorly resolved magnetic HFS of about equal intensity. The doublet absence can be explained with somewhat larger crystallite size (12 nm) in the sample comparing with $Ni_{0.4}Zn_{0.6}Fe_2O_4$ and in 1.5 times lower content of diamagnetic Zn^{2+}. The MS at 78 and 16 K are well fitted with two magnetic HFS of equal intensity indicating the formation of the fully inverted spinel structure. The Mössbauer spectra of $Ni_{0.8}Zn_{0.2}Fe_2O_4$ and $NiFe_2O_4$ with an average crystallites size of 17 nm also demonstrate at 300, 78 and 16 K the superposition of two magnetic HFS of equal intensity indicating the formation the inverted spinel structure. With decrease in temperature, the linewidths of the two components of the magnetic HFS vary little, and B_{in} increases to slightly below the level typical of bulk nickel ferrite observed for nanocrystalline $NiFe_2O_4$ obtained by mechanochemical synthesis [17].

The detailed analysis of the Mössbauer spectra at 16 K allows us to determine the distribution of cations between tetrahedral (*A*) and octahedral (*B*) positions in spinel structure of all samples $Ni_xZn_{1-x}Fe_2O_4$ (Table 2). At such a low temperature lattice vibrations are substantially reduced, so that the probability of the Mössbauer effect for the iron cations in both positions can be considered as the same and the ratio of the populations is equal to the ratio of areas of the sextets. Positions *A* and *B* correspond, respectively, to a sextet with smaller and larger values of B_{in}. Full distribution of cations with the definition of structural formulas was carried out under the assumption that Ni^{2+} occupies only octahedral positions, which is typical for the structure of inverse spinel nickel ferrite $NiFe_2O_4$. Depending on samples composition the tetrahedral positions can be occupied by only Fe^{3+} cations (inverse spinel, $x \geq 0.4$) or by Fe^{3+} and Zn^{2+} cations (mixed spinel, $x=0$, 0.2). Such complicated distribution of cations between tetrahedral and octahedral positions explains the deviation from Vegard's law (Fig. 4) observed for lattice parameter change.

The NH_3–TPD curves of the ferrites $Ni_xZn_{1-x}Fe_2O_4$ are presented in Fig. 6. The density of acid centers A/S_{BET}, i.e. the total amount of acid sites normalized on 1 m^2 of surface area, decreases with increase of nickel content in the ferrites $Ni_xZn_{1-x}Fe_2O_4$ (Table 1). At the same time the addition of nickel results in the decrease of ammonia desorption energy, evidenced by the shift of TPD peaks to lower temperatures.

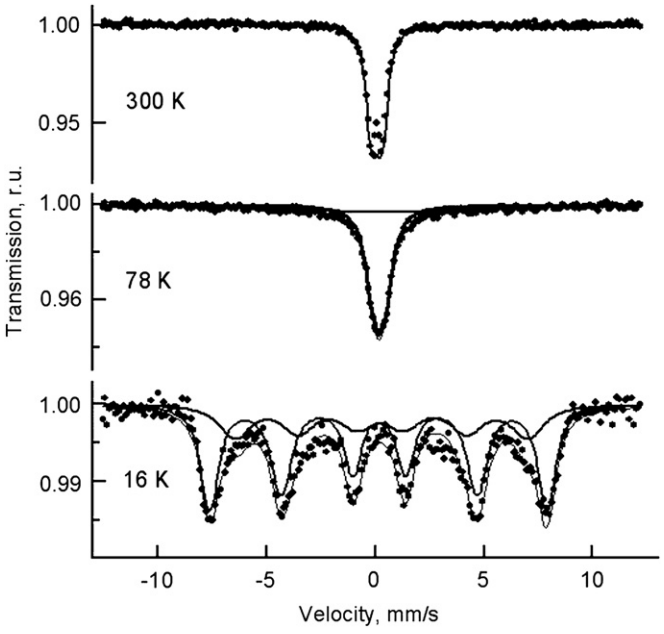

Fig. 5. The Mössbauer spectra of $ZnFe_2O_4$ ($d_{XRD}=9$ nm).

Table 2
The Mössbauer parameters of $Ni_xZn_{1-x}Fe_2O_4$ samples at $T=16$ K and distribution of cations between tetrahedral (*A*) and octahedral (*B*) positions in spinel structure.

x in $Ni_xZn_{1-x}Fe_2O_4$	Fe^{3+} site	δ, mm/s (± 0.02)	ΔE_Q, mm/s (± 0.02)	B_{in}, *T* (± 0.2)	Distribution of cations between tetrahedral (*A*) and octahedral (*B*) positions in spinel structure
0	*A* (30%)	0.52	0.17	41.5	$(Zn^{2+}_{0.4}Fe^{3+}_{0.6})_A[Zn^{2+}_{0.6}Fe^{3+}_{1.4}]_B$
	B (70%)	0.44	0.02	47.8	
0.2	*A* (40%)	0.45	0.10	48.0	$(Zn^{2+}_{0.2}Fe^{3+}_{0.8})_A[Ni^{2+}_{0.2}Zn^{2+}_{0.6}Fe^{3+}_{1.2}]_B$
	B (60%)	0.45	−0.02	50.6	
0.4	*A* (50%)	0.46	0.10	49.5	$(Fe^{3+})_A[Ni^{2+}_{0.4}Zn^{2+}_{0.6}Fe^{3+}_{1.0}]_B$
	B (50%)	0.44	−0.08	52.2	
0.6	*A* (50%)	0.41	0.00	50.3	$(Fe^{3+})_A[Ni^{2+}_{0.6}Zn^{2+}_{0.4}Fe^{3+}_{1.0}]_B$
	B (50%)	0.44	−0.02	53.0	
0.8	*A* (50%)	0.41	0.02	50.4	$(Fe^{3+})_A[Ni^{2+}_{0.8}Zn^{2+}_{0.2}Fe^{3+}_{1.0}]_B$
	B (50%)	0.46	−0.02	53.9	
1.0	*A* (50%)	0.44	0.02	50.6	$(Fe^{3+})_A[Ni^{2+}Fe^{3+}]_B$
	B (50%)	0.40	−0.03	54.7	

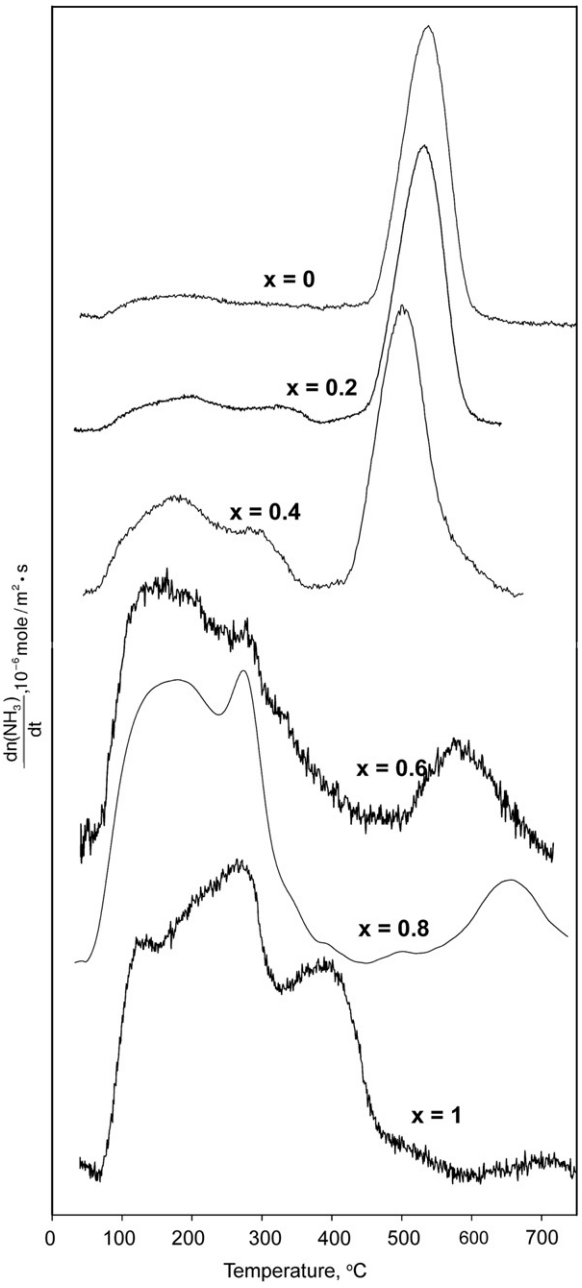

Fig. 6. NH_3–TPD curves of ferrites $Ni_xZn_{1-x}Fe_2O_4$.

Fig. 7 shows the distribution of acid sites by the straight, depending on the composition of ferrites $Ni_xZn_{1-x}Fe_2O_4$. The parts (% of total amount acid centers) of weak, medium and strong sites were estimated from a surface density of acid centers, responsible for NH_3 desorption in the temperature range $T<200$ °C, 200 °C $<T<300$ °C and $T>300$ °C, respectively [18,19]. For ferrites $Ni_xZn_{1-x}Fe_2O_4$, where $x\leq 0.4$, strong acid sites are predominant. With an increase in the nickel content the rise in the part of weak and medium acid sites are observed. For ferrites with $x\geq 0.6$ the number of centers of different strength are comparable.

Surface acidic centers can be divided into two groups: Brønsted centers (hydroxyl groups) and Lewis one (coordinatively unsaturated cations). Portier et al. [20] proposed a parameter related to acid strength of a cation, taking into account the ionic-covalent character of the bond with a base (ionic-covalent

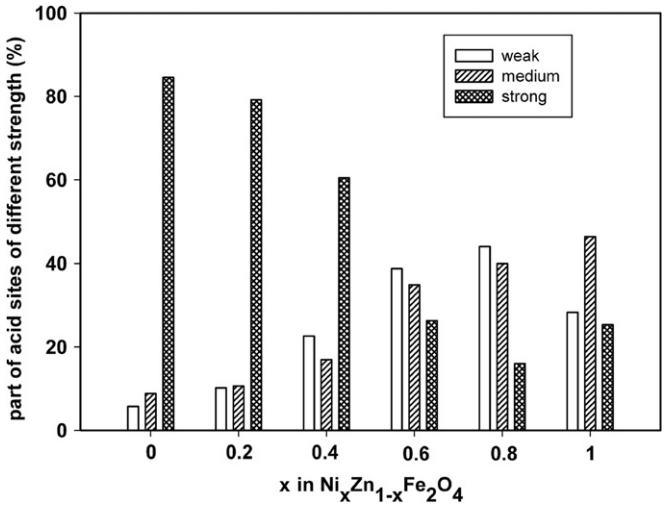

Fig. 7. Distribution of acid sites by the straight, depending on the composition of ferrites $Ni_xZn_{1-x}Fe_2O_4$.

parameter, *ICP*):

$$ICP = \log\left(\frac{z}{r^2}\right) - 1.38\chi + 2.07, \quad (3)$$

where z is the formal cation charge, r is the Shannon ionic radius [7], and χ is electronegativity, taking into consideration the valence and coordination of the cation. *ICP* is a nondimensional number.

The intensity of NH_3 desorption peak at the highest temperature (500–600 °C) is near the same for samples $Ni_xZn_{1-x}Fe_2O_4$ with $x=0$; 0.2; 0.4 and then decreases with the increase of nickel content. Simultaneously the part of zinc cations in octahedral sites in the spinel structure demonstrates the same tendency (Table 2). Such coincidence allows us to conclude that this peak corresponds to desorption of ammonia from zinc cations in the octahedral sites. If we compare the *ICP* values for cations under discussion [20] it can be seen that Zn_B^{2+} is not the strongest Lewis acid in the raw $Ni_B^{2+}(0.525) < Fe_B^{3+}$ $(0.579) < Zn_B^{2+}(0.596) < Zn_A^{2+}(0.718) \approx Fe_A^{3+}(0.719)$. So, it can be assumed that these cations have a stronger chemical interaction with NH_3 molecules due to ammonia dissociative adsorption with the formation of surface NH_2 groups [21].

To characterize the acidic properties of ferrites $Ni_xZn_{1-x}Fe_2O_4$ we summed over all values of *ICP* taking into account the distribution of cations between tetrahedral and octahedral positions in spinel structure (Table 2). For example, for $Ni_{0.2}Zn_{0.8}Fe_2O_4$

$$\Sigma ICP = 0.2ICP(Zn_A^{2+}) + 0.8ICP(Fe_A^{3+}) + 0.2ICP(Ni_B^{2+}) + 0.6ICP(Zn_B^{2+}) + 1.2ICP(Fe_B^{3+}),$$

where *A* and *B* denote tetrahedral and octahedral coordination of cation, respectively. The increase of nickel content leads to decrease of ΣICP that indicates the decrease of acidity of ferrites (Table 1). This assumption is in a good agreement with NH_3–TPD experimental results.

In this work we studied the sensing properties of ferrites $Ni_xZn_{1-x}Fe_2O_4$ towards two different gases: NH_3, which is a typical Lewis base, and C_2H_5OH, which is a molecule with donor and acceptor functional groups.

Fig. 8 shows typical examples of curves obtained from *in situ* conductance measurements, arrows mark the moments of change of the gas mixture. In the temperature range $T<600$ °C oxidation of NH_3 with oxygen chemisorbed on the surface of nanocrystalline

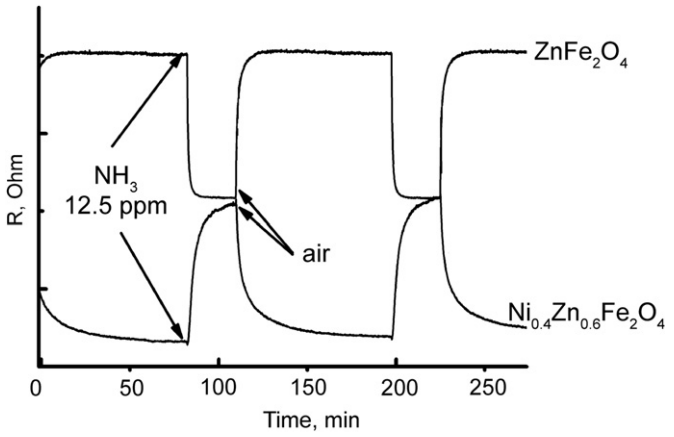

Fig. 8. Change in electrical resistance of $Ni_xZn_{1-x}Fe_2O_4$ during cyclic changes of the gas phase (12.5 ppm NH_3 in air, measurement temperature 350 °C).

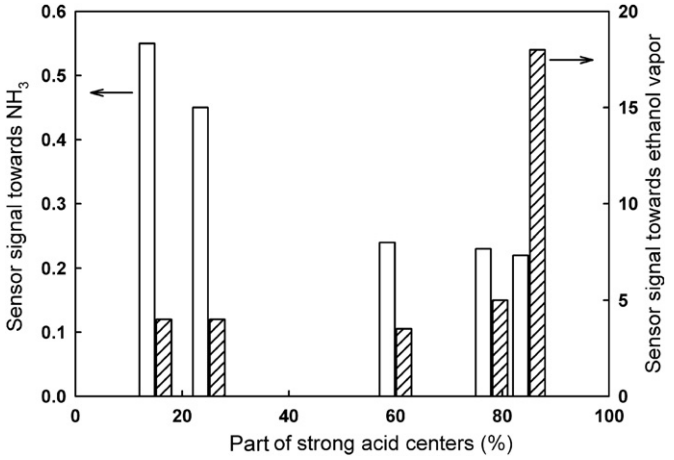

Fig. 9. Sensor signal towards NH_3 and ethanol vapor *vs.* the part of strong acid sites.

oxide materials, can be described by the equation:

$$2\beta NH_{3(gas)} + 3O^{-\alpha}_{\beta(ads)} \rightarrow \beta N_{2(gas)} + 3\beta H_2O_{(gas)} + 3\alpha e^-, \quad (4)$$

where $NH_{3(gas)}$ is the molecule NH_3 in the gas phase, $O^{-\alpha}_{\beta(ads)}$ is particle of chemisorbed oxygen, e^- is electron, which is injected into the conduction band in the reaction, and $N_{2(gas)}$,$H_2O_{(gas)}$ are molecules of reaction products, desorbed into the gas phase.

Interaction of ethanol with the oxides surfaces is quite complicated and sensor signal depends on both the density and nature of surface centers. There are two general ways for ethanol conversion: dehydration and oxidative dehydrogenation [22]. The first one takes place mainly over the surface with the Brønsted acidity and gives a low sensor response. On the contrary, dehydrogenation process needs Lewis acid–basic pairs [23] and leads to a high response due to a reaction with chemisorbed oxygen:

$$\beta C_2H_5OH + O^{\alpha-}_{\beta(ads)} = \beta CH_3CHO + \beta H_2O + \alpha e^- \quad (5)$$

$$\beta CH_3COH_{(gas)} + 5O^{\alpha-}_{\beta(ads)} = 2\beta CO_{2(gas)} + 2\beta H_2O_{(gas)} + 5e^-. \quad (6)$$

Only zinc ferrite reacts for exposure to ammonia and ethanol vapor with the resistance decrease that matches the behavior of *n*-type semiconductor in the presence of reducing gas. Nature of the change in resistance indicates that other synthesized ferrites $Ni_xZn_{1-x}Fe_2O_4$ ($x \geq 0.2$) have *p*-type conduction: electron injection from the reactions (4)–(6) reduces the concentration of holes–the main carrier due to recombination and, consequently, reduce the electrical conductivity of these samples.

Analysis of sensor response depending on the acidic properties of the surface of ferrites $Ni_xZn_{1-x}Fe_2O_4$ (Fig. 9) reveals the following trends. The value of sensor signal towards NH_3 at $T=350$ °C is minimal for the samples with predominant strong acid sites. This may be due to the fact that at this temperature NH_3 molecules are still localized on the strong points Zn_B^{2+}. The bond between these sites and formed NH_2 groups can be interrupted only at higher temperature $T > 500$ °C. So these particles cannot be involved in the oxidation leading to a change in electrical conductivity of the material. Contrary, these strong Lewis acid centers favor ethanol oxidation via dehydrogenation process, which results in a high sensor response.

4. Conclusions

Nanocrystalline ferrites $Ni_xZn_{1-x}Fe_2O_4$ with hierarchical structure were synthesized using aerosol pyrolysis method. The lattice parameter of phase $Ni_xZn_{1-x}Fe_2O_4$ with the spinel structure increases monotonically with increasing *x*. This change correlates with the ionic radii of cations occupying the tetrahedral sites in spinel structure. The detailed analysis of the Mössbauer spectra of all samples $Ni_xZn_{1-x}Fe_2O_4$ allows us to determine the distribution of cations between tetrahedral and octahedral positions in spinel structure. Depending on samples composition the tetrahedral positions can be occupied by only Fe^{3+} cations (inverse spinel, $x \geq 0.4$) or by Fe^{3+} and Zn^{2+} cations (mixed spinel, $x=0$, 0.2). Changing the composition influences the amount and strength of surface acid sites. Increasing the zinc concentration in the ferrite leads to an increase in the number of strong acid centers on the surface. It was found that the decrease in the contribution of strong surface acid sites leads to an increase in sensory sensitivity of the ferrite towards ammonia. For ethanol detection an inverse relationship between sensor signal and surface acidity was observed.

Acknowledgment

The work has financial support by RFBR grants nos. 11-03-00089 and 09-03-00250.

References

[1] C.V. Gopal Reddy, S.V. Manorama, V.J. Rao, J. Mater. Sci. Lett. 19 (2000) 775–778.
[2] M.M. Bucko, K. Haberko, J. Eur. Ceram. Soc. 27 (2007) 723–727.
[3] Yang Liufang, Xie Yongan, Zhao Heyun, et al., Solid-State Electr. 49 (2005) 1029–1033.
[4] K.S. Gavrilenko, T.V. Mironyuk, V.G. Il'in, et al., Theor. Exp. Chem. 38 (2002) 118–124.
[5] E.A. Eremina, A.E. Chekanova, A.P. Kazin, M.N. Rumyantseva, P.E. Kazin, Yu.D. Tretyakov, Inorg. Mater. 43 (8) (2007) 853–859.
[6] A. Tucic, G. Brankovic, Z. Marinkovic, L. Mancic, Chem. Ind. 56 (9) (2002) 375–380.
[7] R.D. Shannon, Acta Crystallogr., Sect. A 32 (1976) 751–767.
[8] A.P. Kazin, M.N. Rumyantseva, V.E. Prusakov, I.P. Suzdalev, Yu.V. Maksimov, V.K. Imshennik, S.V. Novochikhin, A.M. Gaskov, Inorganic Mater. 46 (11) (2010) 1254–1259.
[9] M. Maneva, N. Petrov, J. Therm. Anal. 35 (1989) 2297–2303.
[10] M. Maneva, N. Petroff, M. Pankova, J. Therm. Anal. 36 (1990) 577–587.
[11] N.N. Greenwood, T.G. Webb, Mössbauer Spectroscopy, Chapman and Hall, London, 1971.
[12] W. Schiessl, W. Potzel, H. Karzel, M. Steiner, G.M. Kalvius, A. Martin, M.K. Krause, I. Halevy, J. Gal, W. Schaefer, G. Will, M. Hillberg, R. Waeppling, Phys. Rev. B. 53 (14) (1996) 91–93.
[13] I.P. Suzdalev, V.N. Buravtsev, V.K. Imshennik, Yu.V. Maksimov, V.V. Matveev, S.V. Novochikhin, A.X. Trautwein, H. Winkler, Z. Phys. D 37 (1996) 55–61.
[14] Y.G. Ma, M.Z. Jin, M.L. Liu, G. Chen, Y. Sui, Y. Tian, G.J. Zhang, Y.Q. Jia, Mater. Chem. Phys. 65 (2000) 79–84.

[15] V.I. Goldanskii, V.F. Belov, M.N. Devisheva, V.A. Trukhtanov, Zh. Eksp. Teor. Fiz. 49 (1965) 1681–1687.
[16] Ya. Aiin, E.J. Choi, S. Kim, D.H. An, K.U. Kang, B.-G. Lee, K.S. Baek, H.N. Oak, J. Korean Phys. Soc. 41 (1) (2002) 123–128.
[17] V. Šepelak, I. Bergmann, A. Feldhoff, P. Heitjans, F. Krumeich, D. Menzel, F.J. Litterst, S.J. Campbell, K.D. Becker, J. Phys. Chem. C 111 (2007) 5026–5033.
[18] S.D. Jackson, J.S.J. Hargreaves (Eds.), Metal oxide Catalysis, WILEY-VCH, Weinheim, 2009.
[19] V.V. Yushchenko, Zh. Fiz. Khim. 71 (1997) 628–632.
[20] J. Portier, G. Campet, J. Etourneau, M.C.R. Shastry, B. Tanguy, J. Alloys Comp. 209 (1994) 59–64.
[21] A. Davydov, Molecular Spectroscopy of Oxide Catalyst Surfaces, John Wiley & Sons Ltd., Chichester, 2003.
[22] T. Jinkawa, G. Sakai, J. Tamaki, N. Miura, N. Yamazoe, J. Mol. Catal. A. 155 (2000) 193–200.
[23] N.G. Valente, L.A. Arrua, L.E. Cadus, Appl. Catal. A 205 (2001) 201–214.